NANO LETTERS
Letter
Cite This: Nano Lett. 2019, 19, 8920−8927
pubs.acs.org/NanoLett

Separating Electrons and Donors in $BaSnO_3$ via Band Engineering

Abhinav Prakash,[*,†,⊥] Nicholas F. Quackenbush,[*,‡,⊥] Hwanhui Yun,[†] Jacob Held,[†] Tianqi Wang,[†] Tristan Truttmann,[†] James M. Ablett,[§] Conan Weiland,[‡] Tien-Lin Lee,[∥] Joseph C. Woicik,[‡] K. Andre Mkhoyan,[†] and Bharat Jalan[*,†]

[†]Department of Chemical Engineering and Materials Science, University of Minnesota, Minneapolis, Minnesota 55414, United States

[‡]Materials Measurement Science Division, Material Measurement Laboratory, National Institute of Standards and Technology, Gaithersburg, Maryland 20899, United States

[§]Synchrotron SOLEIL, L'Orme des Merisiers, Boîte Postale 48, St. Aubin 91192 Gif sur Yvette, France

[∥]Diamond Light Source, Ltd., Harwell Science and Innovation Campus, Didcot, Oxfordshire OX11 0DE, United Kingdom

ABSTRACT: Separating electrons from their source atoms in La-doped $BaSnO_3$, the first perovskite oxide semiconductor to be discovered with high room-temperature electron mobility, remains a subject of great interest for achieving high-mobility electron gas in two dimensions. So far, the vast majority of work in perovskite oxides has focused on heterostructures involving $SrTiO_3$ as an active layer. Here we report the demonstration of modulation doping in $BaSnO_3$ as the high room-temperature mobility host without the use of $SrTiO_3$. Significantly, we show the use of angle-resolved hard X-ray photoelectron spectroscopy (HAXPES) as a nondestructive approach to not only determine the location of electrons at the buried interface but also to quantify the width of electron distribution in $BaSnO_3$. The transport results are in good agreement with the results of self-consistent solution to one-dimensional Poisson and Schrödinger equations. Finally, we discuss viable routes to engineer two-dimensional electron gas density through band-offset engineering.

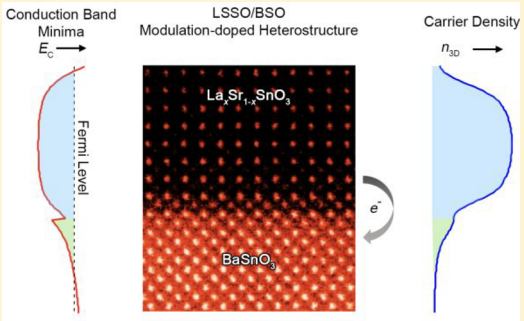

KEYWORDS: *Modulation doping, charge transfer, band alignment, alkaline-earth stannate, transparent conductor, wide band gap material*

Interfaces between perovskite oxides have created tremendous excitement because of the potential for emergent phenomena and novel field-effect devices, resulting in over thousand publications.[1−3] The vast majority of these works focuses on the $LaAlO_3/SrTiO_3$ (LAO/STO)[4−6] interface including some on Al_2O_3/STO[7] and $ReTiO_3$/STO (Re = rare earth element)[1,8,9] interfaces. Amazingly, all of these heterostructures involve the use of STO as an active layer where electron transport occurs.[1,4,5,8] For this reason, room-temperature (RT) electron mobility in these interfaces has always remained <10 $cm^2\ V^{-1}\ s^{-1}$[10−12] and has been ascribed to the strong electron−phonon scattering in STO.[12,13]

Modulation doping is an approach where a semiconductor *A* can be remotely doped by interfacing it with semiconductor *B* that has a higher conduction band minimum. The benefits of modulation doping stem largely from the fact that electrons are spatially separated from their donor ions. Modulation-doped structures in compound semiconductors have yielded two-dimensional electron gases (2DEGs) with outstanding tunability and exceptionally high mobilities both at low temperature and RT.[14,15] Attempts to synthesize non-STO based modulation-doped heterostructure have been unsuccessful so far despite theoretical predictions.[16,17] Nor has any appreciable level of control been gained over the electron density at the interface, which is critical to device applications. A recent report has claimed interface conduction at $BaSnO_3/LaInO_3$ using the polarization-doping approach but modulation doping is yet to be demonstrated in a non-STO-based perovskite heterostructure.[18,19] Even among the STO-based structures, $SrTi_{1-x}Zr_xO_3/SrTiO_3$ is the only system with a successful demonstration of modulation doping but with low RT mobility.[20]

Recently, alkaline earth stannates with perovskite structure have emerged as promising candidates for high RT mobility and high optical transparency.[21−27] High RT electron mobility is attributed to the low electron effective mass and weak electron−phonon interaction.[17,24] $SrSnO_3$ (SSO) possesses wider bandgap (4−4.5 eV) and can be doped *n*-type in thin films with reasonably high electron mobility, 70 $cm^2V^{-1}s^{-1}$ at RT.[28−30] Additionally, SSO films can be grown coherently.[29] $BaSnO_3$ (BSO), on the other hand, possesses a lower bandgap of ∼3 eV,[17,31] a relatively larger lattice parameter (4.116 Å), and has not yet been grown fully strained on a commercially available substrate. The latter introduces misfit and threading

Received: September 16, 2019
Revised: November 1, 2019
Published: November 8, 2019

Downloaded via UNIV OF MINNESOTA on December 12, 2019 at 21:17:03 (UTC).
See https://pubs.acs.org/sharingguidelines for options on how to legitimately share published articles.

© 2019 American Chemical Society

DOI: 10.1021/acs.nanolett.9b03825
Nano Lett. 2019, 19, 8920−8927

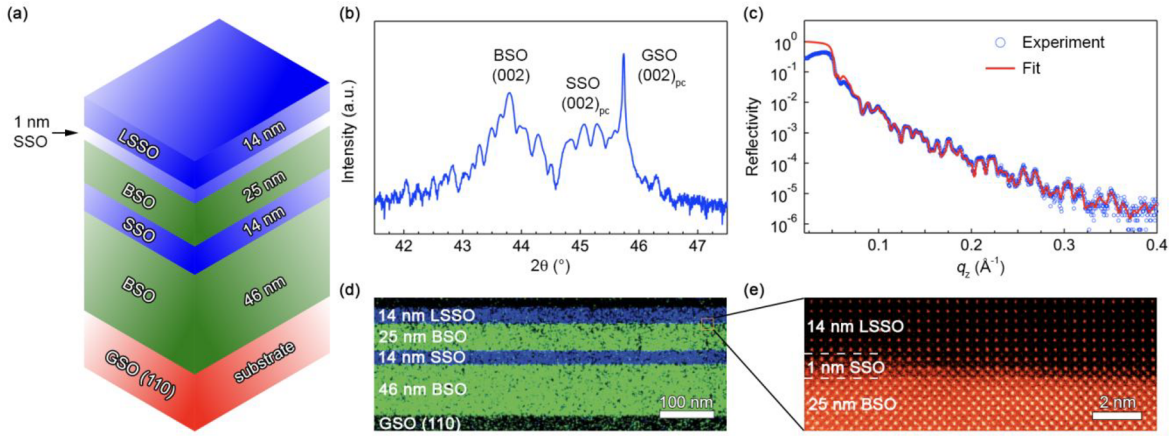

Figure 1. Structural characterization of $SrSnO_3/BaSnO_3$ heterostructure. (a) Schematic of the $SrSnO_3/BaSnO_3$ heterostructure grown on GSO (110), (b) wide-angle X-ray diffraction (WAXRD), (c) grazing incidence X-ray reflectivity of the heterostructure along with a fit using GenX software, (d) energy dispersive X-ray (EDX) elemental maps of Ba L_α (green) and Sr L_α (blue) in the heterostructure, (e) HAADF-STEM image of the top LSSO/SSO/BSO interface.

dislocations in BSO films limiting electron mobilities below that of bulk single crystals.[23−26,32] Although some progress has been made in addressing dislocation issues using undoped buffer layer[23−26,32,33] or by developing lattice-match substrates,[34] very little has been done to eliminate scattering due to ionized donors.

Here, we report the first demonstration of modulation doping approach separating electrons and charged dopants in BSO using a band-engineered heterostructure grown by hybrid molecular beam epitaxy (MBE). We show that the La-doped SSO (LSSO)/BSO system precisely fulfills the theoretical criteria for electron doping in BSO using electrons from LSSO, and we demonstrate how the rearrangement of electrons can be used to control the insulator-to-metal transition in these heterostructure. Using hard X-ray photoelectron spectroscopy (HAXPES), scanning transmission electron microscopy (STEM), and electrical transport, we establish the band alignment, location of electron gas, and their spatial distribution in LSSO/BSO heterostructures in addition to demonstrating insulator-to-metal transition in LSSO owing to an internal charge transfer.

We first present the structural data of the heterostructure investigated in this work. Figure 1a shows the schematic of the heterostructure consisting of $GdScO_3$ (GSO) (110)/46 nm BSO/14 nm SSO/25 nm BSO/1 nm SSO/14 nm LSSO. A 46 nm-thick BSO buffer layer was grown on GSO to obtain a relaxed, insulating BSO film as a template for subsequent film growth. A fully strained 14 nm SSO layer was then grown followed by a 25 nm BSO layer in an attempt to constrain threading dislocations in the bottom BSO buffer layer. An undoped 1 nm SSO was used between BSO and LSSO as a spacer layer to provide a larger spatial separation between charge carriers and donor ions for modulation doping. We note that our rationale for choosing thickness of SSO and LSSO on BSO is 2-fold: to avoid strain relaxation of SSO + LSSO films and to maximize the density of two-dimensional electrons in the BSO channel region. For brevity, we will refer to this structure as LSSO/BSO heterostructure. Figure 1b shows a wide-angle X-ray diffraction (WAXRD) scan of this structure showing (002) film peaks, (002) substrate peak, and thickness fringes. Analysis of the XRD data yielded an out-of-plane lattice parameter of 4.131 Å ± 0.002 Å for BSO layers (mostly relaxed), 4.010 Å ± 0.002 Å for SSO layers consistent with a fully strained SSO film on BSO, and layer thicknesses in excellent agreement with their intended structure as shown in Figure 1a. Grazing incidence X-ray reflectivity (GIXR) scan with well-defined Kiessig fringes (Figure 1c) further confirms uniform film thicknesses consistent with WAXRD data. GenX fits also yielded interface roughness for each interface, <1−2 unit cell (u.c.), which is consistent with our STEM analysis, which combines high-angle annular dark-field (HAADF) imaging with the energy-dispersive X-ray spectroscopy (EDX). The EDX elemental map of Ba L_α (green) and Sr L_α (blue) of the SSO/BSO heterostructure, presented in Figure 1d, shows uniform film thickness and the absence of any phase segregation. In addition, atomic-resolution HAADF STEM image of the top 14 nm LSSO/1 nm SSO/25 nm BSO interface indicates a reasonably smooth interface (Figure 1e) and no presence of misfit dislocations in SSO. However, inspection of STEM images shows a large number of threading dislocations in BSO due to strain relaxation.

We now turn to the discussion of electrical transport data. Figure 2a shows sheet resistance (R_s) versus T plot for LSSO/BSO heterostructures consisting of 14 nm (red solid line) and 7 nm (green solid line) LSSO layers indicating insulating behaviors with $R_s > h/e^2$ at all temperatures. For reference, we also show R_s versus T as an inset for a representative 12 nm LSSO film without a BSO interface layer revealing a metallic behavior with significantly lower sheet resistance. For doping, the La cell temperature was kept fixed at 1200 °C. The observed behavior is significantly different for LSSO when it is interfaced with BSO. This result suggests that electrons are either trapped in structural-related defects in SSO or may have transferred to BSO layer with low mobility accompanied by a metal-to-insulator transition in LSSO. As discussed above, no noticeable structural defects were observed in LSSO film grown on BSO. Rather, our Hall measurements showed nonlinear behavior associated with two-channel conduction.

Figure 2b,c shows transverse resistance, R_{xy} at 30 K as a function of magnetic field (B) revealing a linear Hall slope for the 14 nm LSSO/BSO heterostructure and a nonlinear Hall slope for the sample with 7 nm LSSO layer. Note the dopant density was kept identical in these samples. Although the linear Hall slope does not explicitly rule out two-channel conduction,

DOI: 10.1021/acs.nanolett.9b03825
Nano Lett. 2019, 19, 8920−8927

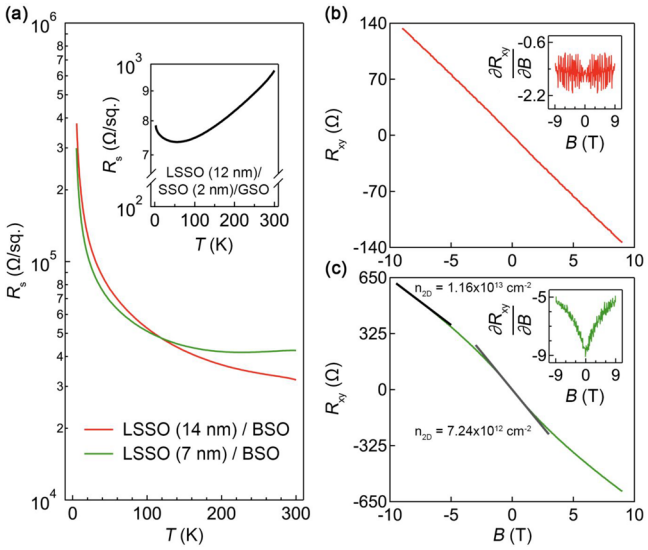

Figure 2. Electrical transport in $SrSnO_3/BaSnO_3$ heterostructures. (a) R_s versus T for the LSSO/BSO heterostructures with −14 nm LSSO (red) and 7 nm LSSO (green). Inset shows the R_s versus T behavior for 12 nm LSSO/2 nm SSO/GSO (110) without BSO interface layer as a reference. (b,c) Transverse resistance (R_{xy}) as a function of B at 30 K for the two heterostructures. Insets show the corresponding first derivatives of R_{xy} with respect to B ($\partial R_{xy}/\partial B$ in mΩ/G) versus B.

the nonlinear behavior in 7 nm LSSO/BSO sample clearly suggests the presence of two-channel conduction. The fitting of nonlinear Hall behavior at low B-field and high B-field yielded a nominal carrier density of 7.24×10^{12} and 1.16×10^{13} cm^{-2}, respectively. The low magnetic field density typically results from high-mobility carriers whereas at high-fields, all carriers can contribute to the Hall signal. Two-channel conduction model did not produce reliable fits to the data given there are four variables. For this reason, we do not report on the results of fitting including the values of electron mobility in two channels. Rather, we estimated carrier density using low-field slope and high-field slope suggesting qualitatively electron density in the order of mid-10^{12} cm^{-2} in the two channels, which is near or below the critical density for metal-to-insulator transition in stannates as reported earlier.[24,35,36] We argue that it is this redistribution of electrons across the interface which makes LSSO/BSO insulating, whereas LSSO without BSO remains metallic. Additionally, interfacial scattering and scattering from threading dislocations in BSO can also play important roles in localizing the carriers. Significantly, however, in agreement with the nonlinear Hall data, HAXPES measurements revealed the electron transfer from LSSO to BSO owing to modulation doping due to a straddling type I band alignment, as discussed below.

To investigate the band alignment, we first measure the valence band (VB) photoemission of the two reference materials as shown in Figure 3a. The VB maxima (E_v) are determined from the linear fit to the leading edge of the main VB and extrapolating it to zero intensity.[37] The small density of states observed between 2 and 3 eV are due to growth-related defects, for example, dislocations and/or point defects. Future investigations will focus on determining the source of midgap states in BSO and SSO films. The VB maxima were found to be 3.99 eV ± 0.02 and 3.18 eV ± 0.02 for LSSO and BSO, respectively. In addition to the VB, the LSSO HAXPES spectrum also displays a weak feature with a sharp edge at the Fermi level (magnified 100×), representing occupied Sn 5s states at the bottom of the conduction band. This is confirmed to be correlated to the presence of La in the core level HAXPES spectrum (see inset) and is analogous to the well-studied La-doping in BSO, due to their similar electronic structure.[38−40] This provides a reasonable estimate of the bandgap of our LSSO, because the conduction band minimum (E_C) is nearly degenerate with E_F, thus $E_V \approx E_G$. Undoped BSO however, does not have this conduction band filling and so E_V can only be considered as a lower limit of the band gap. Our value of 3.18 eV is in good agreement with previous reported thin film samples.[31,41,42] The VB HAXPES spectrum of the LSSO/BSO heterostructure is shown in Figure 3b. Because of the inherent surface sensitivity of photoemission, the VB spectrum is dominated by the top LSSO layer, however the high kinetic energy of HAXPES allows the Ba 5p doublet near 15 eV from the buried BSO layer to be observed. To determine the VB offset at this buried interface, the VB spectrum of the heterostructure is fitted as a linear combination of the spectra collected from each reference material, allowing the binding energy alignment to be determined by the fit. The resulting components of the fit are displayed in Figure 3b with dotted lines. We thus find the VB offset to be 0.71 ± 0.03 eV. Figure 3c shows the energy level flat-band diagram for the heterostructure based on our HAXPES measurements consistent with a conduction band offset of +0.10 eV between LSSO and BSO. It is noted that no error bar is included here due to the unknown uncertainty in the values of the bandgaps. However, our claim of a small positive conduction band offset is clearly supported by our angle-resolved HAXPES and transport measurements as discussed below.

To get further insights into the transport data discussed in Figure 2, we calculated the band diagram using experimental band offsets for the LSSO/BSO heterostructure (Figure 3d). The band diagram was calculated using one-dimensional (1D) Poisson solver.[43] For calculations, dielectric constants of 20 and 17 were used for SSO and BSO, respectively.[44] La dopant density of 8.5×10^{19} cm^{-3} ($n_{2D} = 1.2 \times 10^{14}$ cm^{-2}) in the 14 nm LSSO layer were used. A surface built-in potential of 0.1 eV was used in our calculations to account for surface depletion effect as observed in doped SSO films.[30] We further note that it is this surface potential that leads to the band bending on the surface as shown in Figure 3d. Figure 3d (top panel) reveals the presence of lower potential region (shaded in green) for electrons on the BSO side of the interface in addition to confirming that a fraction of electrons from LSSO can transfer toward the BSO side. Figure 3d (bottom panel) shows the calculated three-dimensional (3D) electron density profile across LSSO/BSO as a function of depth yielding an expected carrier density of 9×10^{13} and 5×10^{12} cm^{-2} on the LSSO and BSO, respectively, as a result of modulation doping and electron transfer. Our result is in good agreement with the DFT calculations.[17]

We look again to HAXPES to investigate the location and spatial distribution of the conduction electrons at E_F. By resolving the emission angle of the ejected photoelectrons, a depth profile can be achieved. Figure 4a shows the angle-integrated (traditional) VB HAXPES spectrum (top) along with the emission-angle resolved two-dimensional (2D) spectrum (bottom). The 2D spectrum was analyzed by dividing into five angular ranges (centered at 82°, 71°, 61°, 51°, and 40°) and summing to create five VB spectra with

DOI: 10.1021/acs.nanolett.9b03825
Nano Lett. 2019, 19, 8920−8927

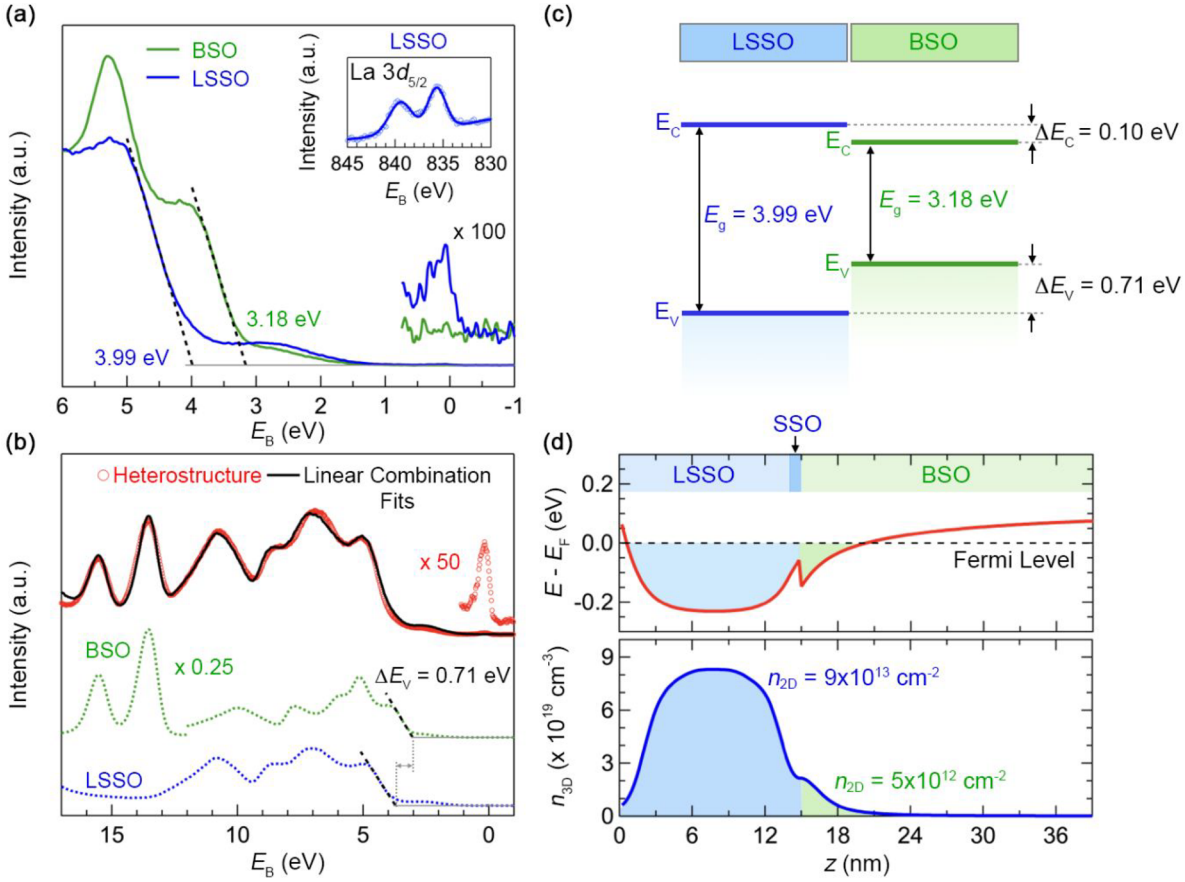

Figure 3. Band alignment at LSSO/SSO/BSO interface. (a) VB spectra of the reference BSO (green) (56 nm BSO/STO (001)) and LSSO (blue) (41 nm LSSO/8 nm SSO/GSO (110)) films. Electronic states near the Fermi states are magnified. Inset shows the La $3d_{5/2}$ core-level X-ray photoelectron spectra, (b) VB spectra of the SSO/BSO heterostructure (red) along with the fit (black) using linear combination of the reference VB spectra (dotted green and blue lines) to determine the VB offset. (c) Energy-level flat-band diagram showing the measured band offsets between LSSO and BSO, and (d) conduction band minima (red) referenced to the Fermi level (top panel) and 3D carrier density, n_{3D} (blue) as a function of depth for the SSO/BSO (bottom panel). The shaded regions indicate 2D density in LSSO and BSO layers after the charge transfer.

varying depth sensitivity. Figure 4c–e shows the extracted shallow core level regions, Sr 4p and Ba 5p, after background removal, as well as the region near E_F, where a small density of states is observed as in the reference LSSO. The intensity profile of these E_F states, shown in Figure 4b, is found to decrease at more surface sensitive angles (smaller emission angle), directly indicating that the majority of this signal originates from beneath the top SSO layer. In fact, the intensity, as a function of the angle, exhibits a profile similar to the Ba 5p of the buried BSO layer, however the weaker exponential decay suggests a more complicated depth profile. We also note that the Ba 5p doublet, shown in Figure 4d, becomes more asymmetric at shallower angles. This could be evidence of a built-in potential as predicted by our 1D Poisson model.[45,46]

To extract more quantitative depth information, these normalized intensity profiles are modeled based on the exponential attenuation of the escaping photoelectrons.[47,48] The intensity of photoelectrons measured at the analyzer is $I = I_0(e^{-t/\lambda \sin \alpha})$, where α is the emission angle, t is the thickness of the overlayer the photoelectrons must traverse, and λ is the effective attenuation length, which can be calculated. Here, λ was calculated to be 7.7 nm for SSO at the photon energy and polarization geometry used via the TPP-2M equation[49,50] and accounting for the single scattering albedo.[51] The Sr 4p and Ba 5p profiles fit well when modeled as arising from the top 15 nm or buried under such a layer, respectively. Following this same analysis for the E_F states, the best fit is found when modeled as a buried layer with the inclusion of a second term representing a finite intensity of these E_F states arising from the top SSO layer, thus

$$I_{EF}(\alpha) = I_0^{\text{int.}}(e^{-t_1/\lambda \sin\alpha} - e^{-(t_1+t_2)/\lambda \sin\alpha}) + I_0^{\text{film}}(1 - e^{-t_1/\lambda \sin\alpha})$$

where t_1 is the thickness of the SSO layer (15 nm) and t_2 is a fit parameter representing the thickness of the interface layer, that is, the top layers of the BSO. The fit reveals a thickness of this interface layer to be about 1.5 nm ±0.5 nm (3–4 u.c.).

Therefore, it is evident that electrons transfer from LSSO to BSO owing to straddling type I band alignment and that these electrons are spread over 3–4 u.c. in BSO. However, one may still argue La interdiffusion from LSSO to BSO to be a source of electrons in BSO buried layer. To eliminate the possibility of interdiffusion, we performed atomic-resolution STEM/EELS analysis of the LSSO/SSO/BSO interface. Figure 5a shows the atomic-resolution annular dark-field (ADF) STEM image of the interface and the positions from where EELS spectra were acquired. Spectra of O K edge, and Ba and La $M_{4,5}$ edges collected across the interface are shown in Figure 5c,d, respectively. Because of a weak EELS signal for Sr, we used fine structure of the O K edge to analyze Sr distribution across the interface. O K spectra marked as bold solid lines in Figure 5c

DOI: 10.1021/acs.nanolett.9b03825
Nano Lett. 2019, 19, 8920–8927

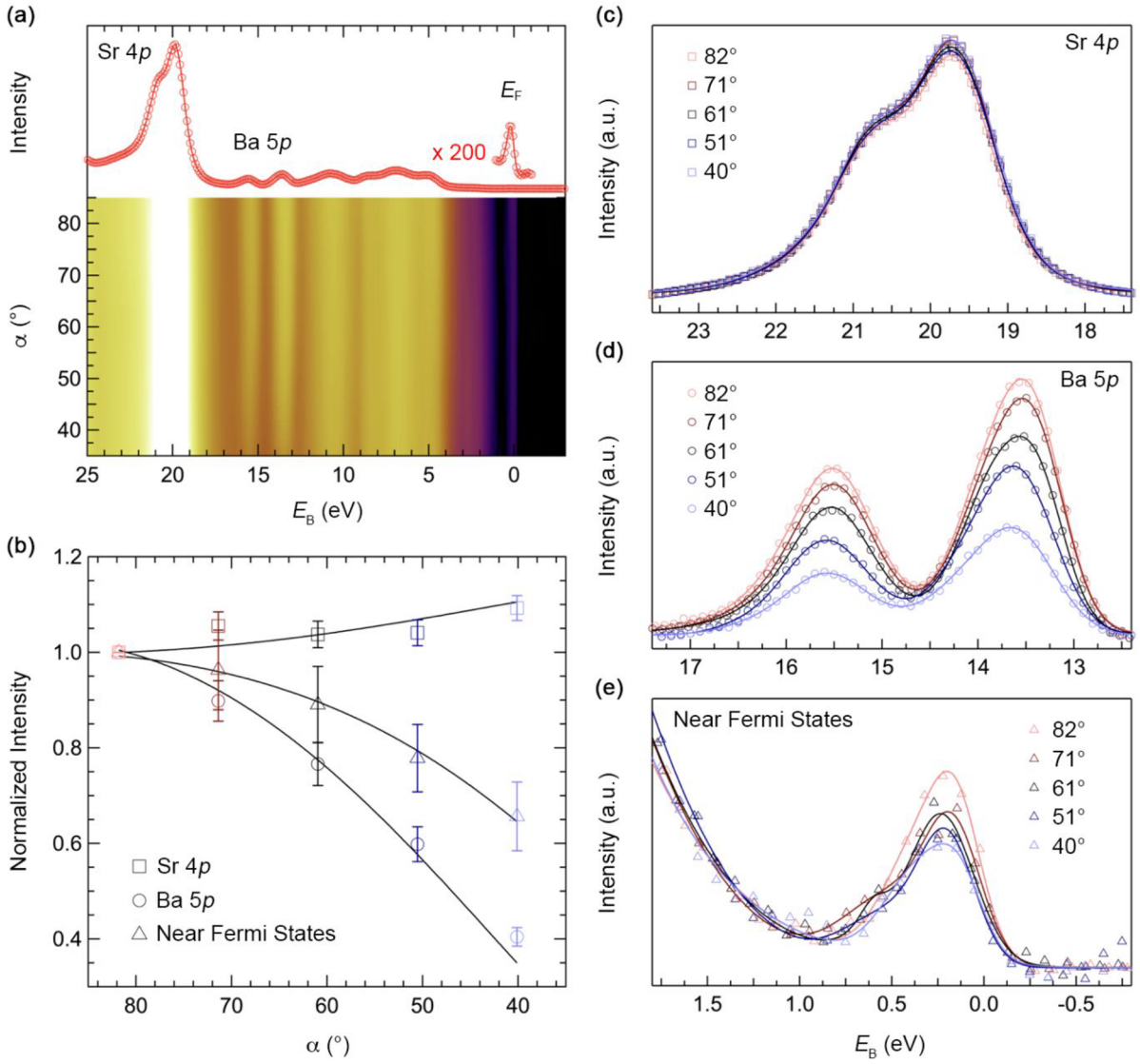

Figure 4. Angle-dependent X-ray photoemission. (a) Angle-resolved HAXPES VB spectrum of LSSO/BSO heterostructure. Integrated intensity over all emission angles is shown in the top panel. (b) Normalized intensity as a function of the emission angle for Sr 4p (squares), Ba 5p (circles) core levels and near Fermi states (triangles). (c−e) Angle-resolved HAXPES spectra of Sr 4p, Ba 5p, and near Fermi states.

were used as a reference for bulk BSO and SSO (regions away from the interface). Figure 5b shows the O *K* edges from the SSO and BSO layers using linear superposition of O *K* edge spectra obtained from bulk SSO and BSO. Figure 5b also depicts Ba- and La-profile across the interface determined from the analysis of EELS data shown in Figure 5d. La concentration was analyzed using the method reported elsewhere.[52] It is noteworthy that Ba-distribution determined from EELS $M_{4,5}$ edge and O *K* edge follows nearly an identical trend confirming the viability of method for determining Sr distribution across the interface. These results show no measurable La concentration in the BSO buried layer providing strong evidence against the interdiffusion as a source of electron in BSO. The La curve follows an error function similar to the O *K* (SSO) profile, albeit shifted ∼1 nm away from BSO, due to the presence of SSO spacer layer.

In summary, we have demonstrated modulation doping in LSSO/BSO heterostructures revealing a straddling type I band offset. Using electrical transport and HAXPES, the transfer of electrons from LSSO to BSO is confirmed which was accompanied by the metal-to-insulator transition in LSSO due to charge distribution. Angle-resolved HAXPES yielded a thickness of 3−4 u.c. over which electrons are spread in BSO. Although we showed electrons were separated from the donor ions, transport in BSO remains limited by threading dislocations and weaker confinement. We argue that LSSO/BSO can provide an ideal model material system for realizing high-mobility 2DEGs in complex oxides at RT if the conduction band offset can be increased either through alloying or strain tuning.

Methods. *Hybrid Molecular Beam Epitaxy of SSO/BSO Heterostructures.* SSO/BSO heterostructures were grown using hybrid molecular beam epitaxy. This approach employs a chemical precursor, hexamethylditin (HMDT), for Sn, conventional solid sources for Sr, Ba, and La (ultrahigh purity of >99.99%), and an RF plasma for oxygen. La was used as an n-type dopant for the doped SSO layer. Films were grown using codeposition in an ultrahigh vacuum MBE chamber (EVO-50, Omicron) with a base pressure of 1.3×10^{-8} Pa (10^{-10} Torr). Beam equivalent pressures (BEP) of 6.7×10^{-6}

DOI: 10.1021/acs.nanolett.9b03825
Nano Lett. 2019, 19, 8920−8927

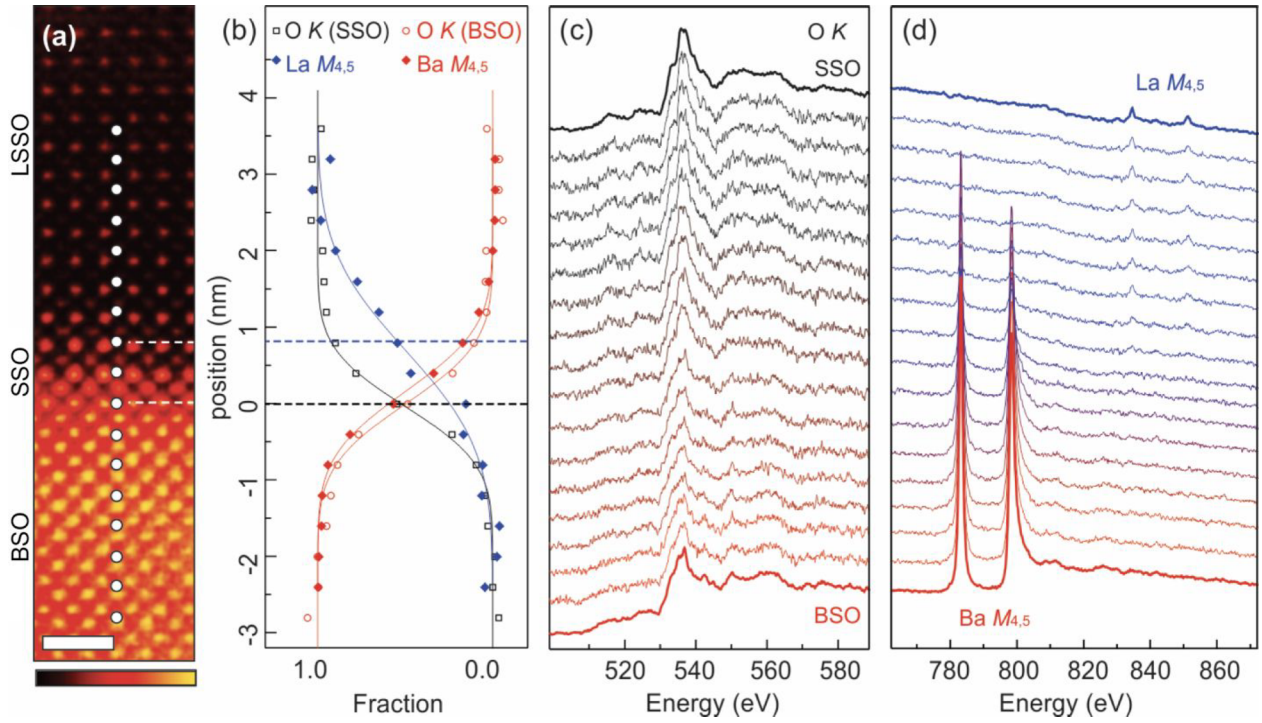

Figure 5. Core-loss STEM-imaging and EELS obtained at the LSSO/SSO/BSO interface. (a) Atomic-resolution ADF-STEM image of the LSSO/SSO/BSO interface of GSO (110)/ 46 nm BSO/14 nm SSO/25 nm BSO/1 nm SSO/14 nm LSSO heterostructure. The white solid circles mark the position where EELS data were acquired. Scale bar is 1 nm. (b) The fraction of each element estimated from core-loss EELS across the interface. EELS spectra from across the interfaces for O *K* edge (c), and Ba and La $M_{4,5}$ edges (d). The results in panel (b) were fitted to a standard error function and the mean positions, (x_0) of the erf($x - x_0$) are marked with dashed lines.

Pa (5×10^{-8} Torr) and 3.3×10^{-4} Pa (2.5×10^{-6} Torr) were used for Ba and HMDT, respectively, for the growth of stoichiometric BSO, whereas BEPs of 4.0×10^{-6} Pa (3×10^{-8} Torr) and 1.3×10^{-4} Pa (1.0×10^{-6} Torr) were used for Sr and HMDT for growth of stoichiometric SSO films. La cell temperature was maintained at 1200 °C during the growth of La-doped SSO layer. An oxygen pressure of 6.7×10^{-4} Pa (5×10^{-6} Torr) was used. The plasma was operated at 250 W with deflection plates kept at 250 V preventing high-energy oxygen ions from reaching the growth surface.

Scanning Transmission Electron Microscopy Sample Preparation and Imaging. The cross-sectional transmission electron microscopy sample was prepared by using FEI Helios Nanolab G4 dual-beam focused ion beam (FIB). The samples were thinned using a 30 kV Ga-ion beam and further polished using a 2 kV Ga-ion beam to minimize FIB-induced damage at the surface. STEM experiments were performed using an aberration-corrected FEI Titan G2 60-300 STEM equipped with a corrected electron optical systems dodecapole corrector (CEOS DCOR), super-X system for energy dispersive X-ray (EDX) spectroscopy, and a monochromated and a Gatan Enfinium ER spectrometer for electron energy-loss spectroscopy (EELS). Annular dark-field STEM images and EDX elemental maps were acquired at 200 kV with a beam current of ∼40 pA, where the semiconvergent angle of the probe was 25 mrad. The inner ADF detector angles were 55 and 96 mrad for ADF and HAADF imaging, respectively. Monochromated STEM-EELS measurements were carried out at 200 keV with screen current of ∼25 pA, where the probe semiconvergent angle was 17 mrad and the EELS collection angle was 29 mrad. Dual EELS mode was used to acquire low-loss, including zero-loss peak (ZLP), and high-loss EELS spectra, simultaneously. Energy dispersion of 0.1 eV per channel was used and the energy resolution was 0.4 eV.

Electronic Transport Measurements and Simulation of Band Alignment. Electronic transport measurements were performed in the van der Pauw geometry using a quantum design physical property measurement system (PPMS Dynacool) to extract the carrier density, sheet resistance, and carrier mobility. Indium was used as an Ohmic contact. Measurements were taken at temperatures between 2 and 300 K and the magnetic field range was −9 T to +9 T. The band alignment between SSO and BSO was simulated using 1D Poisson solver, which solves the Schrodinger and Poisson equation self-consistently.[43] A 0.1 eV Schottky barrier was assumed at the LSSO surface accounting for the surface depletion effect in the calculation of band profile.

Hard Energy X-ray Photoelectron Spectroscopy. HAXPES was performed at beamline I-09 at Diamond Light Source (U.K.) with 5.930 keV photon energy using a Si(111) double crystal monochromator followed by a Si (004) channel-cut high-resolution monochromator. The hemispherical photoelectron analyzer was set to 200 eV pass energy resulting in an overall experimental resolution of 200 meV as determined from fitting a Fermi function to the VB of a reference gold foil. The binding energy axis was calibrated using the Fermi level and Au 4f core lines of the gold foil in electrical contact with the sample. The X-rays were 10° glancing incidence on the sample surface and the cone of the photoelectron analyzer was oriented parallel to the polarization vector of the incident X-ray beam. Angle-resolved VB HAXPES was performed in a fixed geometry using a wide-angle lensing mode for parallel detection of photoelectrons over a range of ∼56° with the X-ray incidence angle fixed at 30°.

DOI: 10.1021/acs.nanolett.9b03825
Nano Lett. 2019, 19, 8920−8927

AUTHOR INFORMATION

Corresponding Authors

*E-mail: (A.P.) praka019@umn.edu.
*E-mail: (N.F.Q.) nicholas.quackenbush@nist.gov.
*E-mail: (B.J.) bjalan@umn.edu.

ORCID

Abhinav Prakash: 0000-0002-8899-0568
Jacob Held: 0000-0003-3864-4314
K. Andre Mkhoyan: 0000-0003-3568-5452
Bharat Jalan: 0000-0002-7940-0490

Author Contributions

⊥A.B. and N.F.Q contributed equally.

Notes

The authors declare no competing financial interest.

Disclaimer: The inclusion of company names is for completeness and does not represent an endorsement by the National Institute of Standards and Technology.

ACKNOWLEDGMENTS

The authors thank C. J. Powell for discussions regarding effective attenuation length calculations. This work was primarily supported through the Young Investigator Program of the Air Force Office of Scientific Research (AFOSR) through Grant FA9550-16-1-0205 and in part through Grant FA9550-19-1-0245. Part of this work is supported by the National Science Foundation through DMR-1741801 and partially by the UMN MRSEC program under Award No. DMR-1420013. Parts of this work were carried out in the Characterization Facility, University of Minnesota, which receives partial support from NSF through the MRSEC program. Portions of this work were conducted in the Minnesota Nano Center, which is supported by the National Science Foundation through the National Nano Coordinated Infrastructure Network (NNCI) under Award Number ECCS-1542202. A.P. acknowledges support from University of Minnesota Doctoral Dissertation Fellowship. We also acknowledge partial support from the renewable development funds (RDF) of the Institute on the Environment (UMN) and the Norwegian Centennial Chair Program seed funds. Parts of this research were performed while N.F.Q. held a National Institute of Standards and Technology (NIST) National Research Council (NRC) Research Postdoctoral Associateship Award at the Material Measurement Lab. We thank Diamond Light Source for access to beamline I-09 (SI15845-1) that contributed to the results presented here.

REFERENCES

(1) Stemmer, S.; Allen, S. J. *Annu. Rev. Mater. Res.* **2014**, *44*, 151.
(2) Ramesh, R.; Schlom, D. *MRS Bull.* **2008**, *33*, 1006.
(3) Mannhart, J.; Herrnberger, A. *Nat. Mater.* **2012**, *11*, 91.
(4) Ohtomo, A.; Hwang, H. Y. *Nature* **2004**, *427*, 423.
(5) Mannhart, J.; Blank, D. H. A.; Hwang, H. Y.; Millis, A. J.; Triscone, J. M. *MRS Bull.* **2008**, *33*, 1027.
(6) Chen, Y. Z.; Trier, F.; Wijnands, T.; Green, R. J.; Gauquelin, N.; Egoavil, R.; Christensen, D.; Koster, G.; Huijben, M.; Bovet, N.; Macke, S.; He, F.; Sutarto, R.; Andersen, N. H.; Sulpizio, J. A.; Honig, M.; Prawiroatmodjo, G. E. D. K.; Jespersen, T. S.; Linderoth, S.; Ilani, S.; Verbeeck, J.; Van Tendeloo, G.; Rijnders, G.; Sawatzky, G. A.; Pryds, N. *Nat. Mater.* **2015**, *14*, 801.
(7) Chen, Y. Z.; Bovet, N.; Trier, F.; Christensen, D. V.; Qu, F. M.; Andersen, N. H.; Kasama, T.; Zhang, W.; Giraud, R.; Dufouleur, J.; Jespersen, T. S.; Sun, J. R.; Smith, A.; Nygard, J.; Lu, L.; Buchner, B.; Shen, B. G.; Linderoth, S.; Pryds, N. *Nat. Commun.* **2013**, *4*, 1371.
(8) Xu, P.; Droubay, T. C.; Jeong, J. S.; Mkhoyan, K. A.; Sushko, P. V.; Chambers, S. A.; Jalan, B. *Adv. Mater. Interfaces* **2016**, *3* (2), 1500432.
(9) Xu, P.; Ayino, Y.; Cheng, C.; Pribiag, V. S.; Comes, R. B.; Sushko, P. V.; Chambers, S. A.; Jalan, B. *Phys. Rev. Lett.* **2016**, *117*, 106803.
(10) Prakash, A.; Jalan, B., Molecular Beam Epitaxy for Oxide Electronics In *Molecular Beam Epitaxy: Materials and Applications for Electronics and Optoelectronics*; Asahi, H., Horikoshi, Y., Eds.; Wiley and Sons, 2019; p 423.
(11) Ismail-Beigi, S.; Walker, F. J.; Cheong, S.-W.; Rabe, K. M.; Ahn, C. H. *APL Mater.* **2015**, *3* (6), 062510.
(12) Verma, A.; Kajdos, A. P.; Cain, T. A.; Stemmer, S.; Jena, D. *Phys. Rev. Lett.* **2014**, *112*, 216601.
(13) Zhou, J.-J.; Hellman, O.; Bernardi, M. *Phys. Rev. Lett.* **2018**, *121*, 226603.
(14) Kroemer, H. *Rev. Mod. Phys.* **2001**, *73*, 783.
(15) Schlom, D. G.; Pfeiffer, L. N. *Nat. Mater.* **2010**, *9*, 881.
(16) Bjaalie, L; Himmetoglu, B; Weston, L; Janotti, A; Van de Walle, C G *New J. Phys.* **2014**, *16* (2), 025005.
(17) Krishnaswamy, K.; Bjaalie, L.; Himmetoglu, B.; Janotti, A.; Gordon, L.; Van de Walle, C. G. *Appl. Phys. Lett.* **2016**, *108* (8), 083501.
(18) Kim, U.; Park, C.; Kim, Y. M.; Shin, J.; Char, K. *APL Mater.* **2016**, *4*, 071102.
(19) Kim, Y.; Kim, Y. M.; Shin, J.; Char, K. *APL Mater.* **2018**, *6*, 096104.
(20) Kajdos, A. P.; Ouellette, D. G.; Cain, T. A.; Stemmer, S. *Appl. Phys. Lett.* **2013**, *103* (8), 082120.
(21) Luo, X.; Oh, Y. S.; Sirenko, A.; Gao, P.; Tyson, T. A.; Char, K.; Cheong, S. W. *Appl. Phys. Lett.* **2012**, *100* (17), 172112.
(22) Kim, H. J.; Kim, U.; Kim, H. M.; Kim, T. H.; Mun, H. S.; Jeon, B.-G.; Hong, K. T.; Lee, W.-J.; Ju, C.; Kim, K. H.; Char, K. *Appl. Phys. Express* **2012**, *5* (6), 061102.
(23) Prakash, A.; Xu, P.; Wu, X.; Haugstad, G.; Wang, X.; Jalan, B. *J. Mater. Chem. C* **2017**, *5* (23), 5730−5736.
(24) Prakash, A.; Xu, P.; Faghaninia, A.; Shukla, S.; Ager, J. W., III; Lo, C. S.; Jalan, B. *Nat. Commun.* **2017**, *8*, 15167.
(25) Raghavan, S.; Schumann, T.; Kim, H.; Zhang, J. Y.; Cain, T. A.; Stemmer, S. *APL Mater.* **2016**, *4* (1), 016106.
(26) Paik, H.; Chen, Z.; Lochocki, E.; Seidner, H. A.; Verma, A.; Tanen, N.; Park, J.; Uchida, M.; Shang, S. L.; Zhou, B.-C.; Brützam, M.; Uecker, R.; Liu, Z.-K.; Jena, D.; Shen, K. M.; Muller, D. A.; Schlom, D. G. *APL Mater.* **2017**, *5* (11), 116107.
(27) Arezoomandan, S.; Prakash, A.; Chanana, A.; Yue, J.; Mao, J.; Blair, S.; Nahata, A.; Jalan, B.; Sensale-Rodriguez, B. *Sci. Rep.* **2018**, *8* (1), 3577.
(28) Wang, T.; Thoutam, L. R.; Prakash, A.; Nunn, W.; Haugstad, G.; Jalan, B. *Phys. Rev. Mater.* **2017**, *1* (6), 061601.
(29) Wang, T.; Prakash, A.; Dong, Y.; Truttmann, T.; Bucsek, A.; James, R.; Fong, D. D.; Kim, J.-W.; Ryan, P. J.; Zhou, H.; Birol, T.; Jalan, B. *ACS Appl. Mater. Interfaces* **2018**, *10*, 43802.
(30) Truttmann, T.; Prakash, A.; Yue, J.; Mates, T. E.; Jalan, B. *Appl. Phys. Lett.* **2019**, *115*, 152103.
(31) Chambers, S. A.; Kaspar, T. C.; Prakash, A.; Haugstad, G.; Jalan, B. *Appl. Phys. Lett.* **2016**, *108* (15), 152104.
(32) Lee, W.-J.; Kim, H. J.; Kang, J.; Jang, D. H.; Kim, T. H.; Lee, J. H.; Kim, K. H. *Annu. Rev. Mater. Res.* **2017**, *47*, 391.
(33) Lee, W.-J.; Kim, H. J.; Sohn, E.; Kim, T. H.; Park, J.-Y.; Park, W.; Jeong, H.; Lee, T.; Kim, J. H.; Choi, K.-Y.; Kim, K. H. *Appl. Phys. Lett.* **2016**, *108*, 082105.
(34) Uecker, R.; Bertram, R.; Brutzam, M.; Galazka, Z.; Gesing, T. M.; Guguschev, C.; Klimm, D.; Klupsch, M.; Kwasniewski, A.; Schlom, D. G. *J. Cryst. Growth* **2017**, *457*, 137.
(35) Thoutam, L. R.; Yue, J.; Prakash, A.; Wang, T.; Elangovan, K. E.; Jalan, B. *ACS Appl. Mater. Interfaces* **2019**, *11*, 7666.
(36) Fujiwara, K.; Nishihara, K.; Shiogai, J.; Tsukazaki, A. *Appl. Phys. Lett.* **2017**, *110* (20), 203503.

DOI: 10.1021/acs.nanolett.9b03825
Nano Lett. 2019, 19, 8920−8927

(37) Kraut, E. A.; Grant, R. W.; Waldrop, J. R.; Kowalczyk, S. P. *Phys. Rev. Lett.* **1980**, *44* (24), 1620−1623.
(38) Liu, H.-R.; Yang, J.-H.; Xiang, H. J.; Gong, X. G.; Wei, S.-H. *Appl. Phys. Lett.* **2013**, *102* (11), 112109.
(39) Scanlon, D. O. *Phys. Rev. B: Condens. Matter Mater. Phys.* **2013**, *87* (16), 161201.
(40) Sallis, S.; Scanlon, D. O.; Chae, S. C.; Quackenbush, N. F.; Fischer, D. A.; Woicik, J. C.; Guo, J. H.; Cheong, S. W.; Piper, L. F. J. *Appl. Phys. Lett.* **2013**, *103* (4), 042105.
(41) Lebens-Higgins, Z.; Scanlon, D. O.; Paik, H.; Sallis, S.; Nie, Y.; Uchida, M.; Quackenbush, N. F.; Wahila, M. J.; Sterbinsky, G. E.; Arena, D. A.; Woicik, J. C.; Schlom, D. G.; Piper, L. F. J. *Phys. Rev. Lett.* **2016**, *116* (2), 027602.
(42) Zhang, J.; Han, S.; Luo, W.; Xiang, S.; Zou, J.; Oropeza, F. E.; Gu, M.; Zhang, K. H. L. *Appl. Phys. Lett.* **2018**, *112* (17), 171605.
(43) Tan, I. H.; Snider, G. L.; Chang, L. D.; Hu, E. L. *J. Appl. Phys.* **1990**, *68* (8), 4071−4076.
(44) Nunn, W.; Prakash, A.; Bhowmik, A.; Haislmaier, R.; Yue, J.; Garcia Lastra, J. M.; Jalan, B. *APL Mater.* **2018**, *6* (6), 066107.
(45) Du, Y.; Sushko, P. V.; Spurgeon, S. R.; Bowden, M. E.; Ablett, J. M.; Lee, T.-L.; Quackenbush, N. F.; Woicik, J. C.; Chambers, S. A. *Phys. Rev. Mater.* **2018**, *2*, 094602.
(46) Lim, Z. H.; Quackenbush, N. F.; Penn, A. N.; Chrysler, M.; Bowden, M.; Zhu, Z.; Ablett, J. M.; Lee, T.-L.; LeBeau, J. M.; Woicik, J. C.; Sushko, P. V.; Chambers, S. A.; Ngai, J. H. *Phys. Rev. Lett.* **2019**, *123*, 026805.
(47) Chambers, S. A., Probing Perovskite Interfaces and Superlattices with X-ray Photoemission Spectroscopy. In *Hard X-ray Photoelectron Spectroscopy (HAXPES)*; Woicik, J., Ed.; Springer International Publishing, 2016; pp 341−380.
(48) Sing, M.; Berner, G.; Goß, K.; Müller, A.; Ruff, A.; Wetscherek, A.; Thiel, S.; Mannhart, J.; Pauli, S. A.; Schneider, C. W.; Willmott, P. R.; Gorgoi, M.; Schäfers, F.; Claessen, R. *Phys. Rev. Lett.* **2009**, *102* (17), 176805.
(49) Tanuma, S.; Powell, C. J.; Penn, D. R. *Surf. Interface Anal.* **1994**, *21* (3), 165−176.
(50) Jablonski, A. *Surf. Sci.* **2018**, *667*, 121−137.
(51) Jablonski, A. *J. Phys. D: Appl. Phys.* **2015**, *48* (7), 075301.
(52) Held, J.; Yun, H.; Mkhoyan, K. A. **2019**, arXiv:1906.06379v1.

DOI: 10.1021/acs.nanolett.9b03825
Nano Lett. 2019, 19, 8920−8927